University of New Hampshire
University of New Hampshire Scholars' Repository

Master's Theses and Capstones Student Scholarship

Spring 2013

Investigation of thermal and mechanical effects during electrically-assisted microforming

Adam Jordan
University of New Hampshire, Durham

Follow this and additional works at: https://scholars.unh.edu/thesis

Recommended Citation
Jordan, Adam, "Investigation of thermal and mechanical effects during electrically-assisted microforming" (2013). *Master's Theses and Capstones*. 792.
https://scholars.unh.edu/thesis/792

This Thesis is brought to you for free and open access by the Student Scholarship at University of New Hampshire Scholars' Repository. It has been accepted for inclusion in Master's Theses and Capstones by an authorized administrator of University of New Hampshire Scholars' Repository. For more information, please contact nicole.hentz@unh.edu.

INVESTIGATION OF THERMAL AND MECHANICAL EFFECTS DURING ELECTRICALLY-ASSISTED MICROFORMING

BY

ADAM JORDAN

Bachelor of Science, University of New Hampshire

MASTER THESIS

Submitted to the University of New Hampshire

in Partial Fulfillment of

the Requirements for the Degree of

Master of Science

In

Mechanical Engineering

May, 2013

UMI Number: 1523797

All rights reserved

INFORMATION TO ALL USERS
The quality of this reproduction is dependent upon the quality of the copy submitted.

In the unlikely event that the author did not send a complete manuscript
and there are missing pages, these will be noted. Also, if material had to be removed,
a note will indicate the deletion.

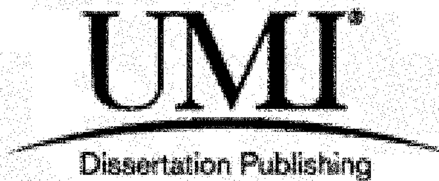

UMI 1523797
Published by ProQuest LLC 2013. Copyright in the Dissertation held by the Author.
Microform Edition © ProQuest LLC.
All rights reserved. This work is protected against
unauthorized copying under Title 17, United States Code.

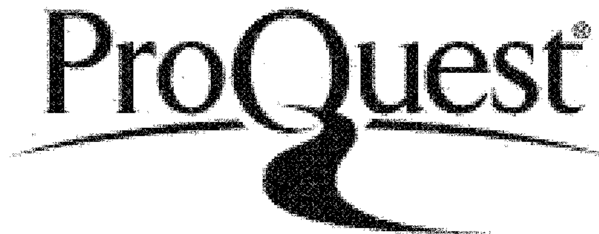

ProQuest LLC
789 East Eisenhower Parkway
P.O. Box 1346
Ann Arbor, MI 48106-1346

This thesis has been examined and approved by

Thesis Director: Brad Kinsey
Professor of Mechanical Engineering

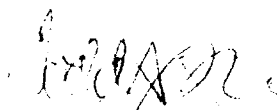

Todd Gross
Professor of Mechanical Engineering

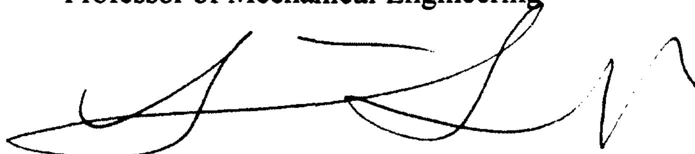

Yaning Li
Professor of Mechanical Engineering

5/17/13
Date:

Dedicated to Gil (Boompa)

ACKNOLWEGMENTS

Funding from U.S. National Science Foundation (CMII-0644705) is gratefully acknowledged

I would first like to thank my advisor, Brad Kinsey for his support, Knowledge and patience with me throughout my college career. Help from Sheldon Parent, Robert Champlin, Adam Perkins and Tracey Harvey is also greatly appreciated.

I would also like to thank my parents, Mark and Diane. Without them I would never be where I am today. I don't think any words here could do their contributions justice.

Lastly I would like to thank Joseph and Ashley. I know much of my life would be different if I had never met you two. Thank you for always being there.

ABSTRACT

INVESTIGATION OF THERMAL AND MECHANICAL EFFECTS DURING ELECTRICALLY-ASSISTED MICROFORMING

By

Adam G. Jordan

University of New Hampshire, May 2013

Degree Advisor: Brad Kinsey

The goal of this research was to investigate Electrically-Assisted Forming (EAF) at the microscale. Past research has suggested that EAF has the potential to overcome microforming difficulties (i.e., increased data scatter caused by the individual grains affecting the global material properties). In this thesis, three point bending results are presented for both classical (non-EA) and EA processes with CuZn30 specimens containing different grain sizes. A more uniform strain distribution was achieved with the EA processes. Although the application of current did not result in the expected forming force reduction, a decrease was observed where a temperature spike occurred (believed to be caused by varying electrical contact).

In addition to the microbending tests, stationary copper wire temperature tests under compression were also performed. Past research had shown the effect of grain size and Zn content during EAF. However, temperature data of the specimens during the tests was not available.

Table of Contents

INTRODUCTION 1
1.1 Why Microforming is Relevant 1
1.2 Major Problems With Microforming 2
1.3 Potential for Electrically-Assisted Forming to Overcome Microforming Difficulties 5
1.4 Brief Overview of EA Forming 6
CHAPTER 2: Three Point Micro Bending 10
2.1 Experimental Methods 10
2.2 Results 22
CHAPTER 3: Copper wire temperature tests 37
3.1 Copper Wire Test Motivation 37
3.2 Experimental Methods 37
3.3 Results 39
CHAPTER 4: Discussion 42
CHAPTER 5: Conlusions 48
5.1 Three Point Microbending 48
5.2 Copper Wire Temperature Tests 49
FUTURE WORK 50
REFERENCES 51

INTRODUCTION

1.1 Why Microforming is Relevant

In the last few decades, several industries have witnessed a major trend towards miniaturization of components and systems. The market for Micro-Electrical Mechanical Systems (MEMS) has grown 17% to a worth of $10.2 billion worth since 2011 (Solid State Technologies, 2012) and is still showing signs of increasing. Even just within the MEMS market for pressure sensors in medical electronics, a growth of 7% is projected within the next year and will reach a projected revenue of $186.7 million by 2016 (Semi, 2012). This growth in turn has lead to the need to produce components at the microscale.

One way microscale parts can be characterized is by having two or more features/dimensions in the micron range (Geiger et al., 2001) or, for metal components, by having fewer than 10 grains through the feature dimension (Hansen et al., 1977). Multiple techniques exist to fabricate parts and components at this scale. For example, photolithography on a silicon substrate has been used to fabricate microstructures. However, this process is limited to 2 ½ D structures (i.e. planar structures with limited out of plane construction) and low potential aspect ratios (Asad et al., 2007). Furthermore, the maximum achievable thickness when using photolithography is relatively small, approximately 100[μm]. Finally, the process is performed only on planar surfaces. Other processes include deep X-ray lithography using synchrotron radiation beam, which is also known as the LIGA process, and the focused-ion beam machining process which can produce 3D sub-micron features with high accuracy. However, these processes require expensive and special facilities.

Conventional machining techniques have also been used to produce metallic parts on the microscale. Micromachining has the advantage of fabricating 3D parts. Although the accuracy of micromachining is excellent, there are undesirable costs associated with tool wear and the time lost while tools are being replaced. There are also issues with simply scaling knowledge of macromachining down to the microscale due to material property changes. More on this effect will be presented in Section 1.2. As at the macroscale, microforming processes (such as compression, bending, etc.) are a low cost, high cycle rate solution for forming microscale components.

1.2 Major Problems With Microforming

At the microscale, the individual grains of the material and features of the component (e.g., surface roughness) have a significant effect on the overall mechanical response and other parameters. Such "size effects" present new challenges with decreased formability and varied material properties. For example Raulea et al. (2001) observed changes in both the tensile and bending yield strengths for aluminum sheet metal with a thickness ranging from 0.17[mm] to 2[mm] (Figure 1). The cause of these changes is the anisotropy of the mechanical properties due to the orientation and properties of individual grains having a larger effect as there are less of them through the thickness. The effect of individual grains in the material is also shown by the increase of the yield strength for thickness to grain ratios under one (obtained by measuring the planar grain size and dividing into thickness). At thickness-to-grain ratios less than one, the mechanical properties of that individual grain through the thickness would determine the overall properties of the specimen, hence the increased scatter at lower thickness to grain ratios.

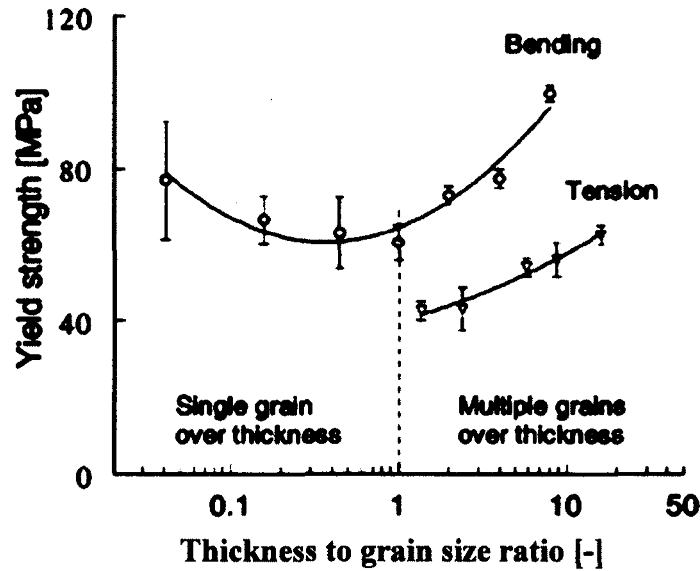

Figure 1: Variation of tension and bending yield strengths with varying thickness to grain size ratio. (Raulea et al., 2001)

Size effects have also been shown to effect how a component will deform. For example, Wang et al. (2011) found that the strain gradients became less steep with miniaturization for specimens with varying grain sizes (i.e. 2-4, 10-15 and 25-30 grains through the thickness representing fine, medium and coarse grain structures respectively) and dimensions (i. e., thicknesses of 0.25, 0.5 and 1.588[mm] with process dimensions scaled by the law of similarity). This would affect the final dimensions of specimens due to springback. See Figure 2 for such varying strain gradients for 3-point microbending of CuZn30 specimens with a thickness of 0.5[mm]. Note that as with other past research results, data scatter increased and flow stress decreased with miniaturization.

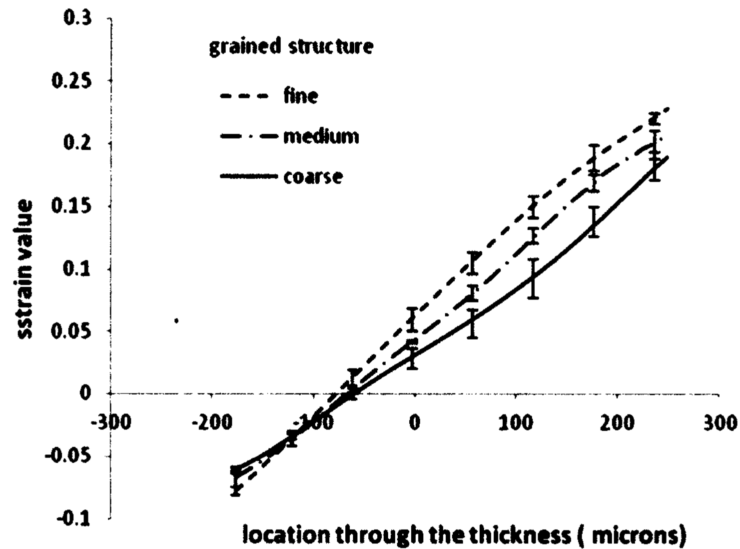

Figure 2: Strain gradients through 0.5 mm thick CuZn30, 3-point microbending specimens. (Wang et al., 2011)

As for springback (i. e., the elastic recovery of the material after the load is removed), Gau et al. (2007) observed an increase in springback angle in Brass 26000 1/2 Hard (H02) specimens after free bending as the average grain diameter approached the thickness of the specimen. Similarly, Diehl et al. (2005) observed an almost three times higher springback angle in aluminum (Al 99.5) foil specimens when the thickness changed from 200[μm] to 25[μm] during a free bending process. These variations in material properties, strain gradient and increase in springback makes mass production of microcomponents difficult.

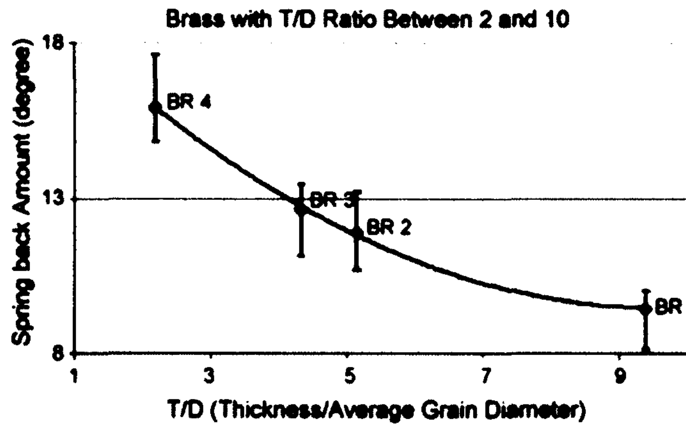

Figure 3: Springback in brass sheet specimens with various grain structures. (Gau et al., 2007)

1.3 Potential for Electrically-Assisted Forming to Overcome Microforming Difficulties

Past research has shown that electrically-assisted (EA) forming has the potential to overcome the various forming difficulties that have been observed with microforming. For example, spring back was completely eliminated at the macroscale by Roth et al. (2001) after a current density of $120[\frac{A}{mm^2}]$ was applied to 0. 91[mm] thick sheets of Al-6111 after forming. Also on the macroscale, Salandro et al. (2010) measured a 5% reduction in springback when electric current was pulsed during bending stainless steel specimens (Figure 4). In addition Perkins et al. (2007) observed force reductions and increased elongations prior to failure for various materials including Aluminum (6061) and Titanium (6Al-4V) alloys.

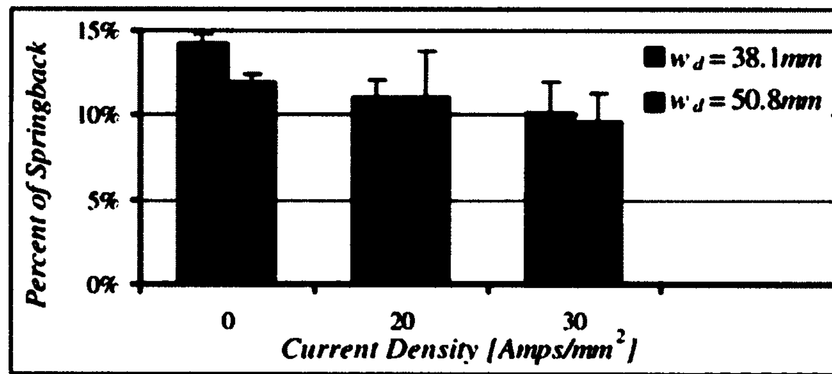

Figure 4: Springback reduction in EA pulsed stainless steel sheets. (Salandro et al., 2010)

Researchers at Clemson University have conducted several studies on the positive effects of EAF. For example Jones and Mears (2010) observed a reduction in forming force when pulsing 304 stainless steel specimens with electrical current during a bending process. Similarly Mears et al. (2012) studied the effects of electrical current on the formability of Mg AZ31B-O round stock (7.94[mm] in diameter). Not only was a major reduction in forming force observed, but the specimen could be compressed over five times more before failure at a current density of $40[\frac{A}{mm^2}]$. The mode of failure also changed from a shear failure for the baseline tests to cracking at lower current densities ($20[\frac{A}{mm^2}]$). Note that the specimens formed at the current density $40[\frac{A}{mm^2}]$ of did not fracture or crack. The application of electrical current also negated the effects of forming speed at higher current densities. For a current density $40[\frac{A}{mm^2}]$ there was no difference in forming depth when the forming rate was varied from 25.4 to $50.8[\frac{mm}{min}]$.

1.4 A Brief Review of EA Forming

Although the effect of electrical current on material properties has been observed as far back as 1889 (Bottomley, 1889), there is still some debate as to what is affecting the material. Research points towards an electroplastic effect (Conrad, 2000) that exceeds the

effects that can be explained just by resistive heating (i.e., hot working) alone. The theories proposed to explain this effect focus on the fundamental mechanism of plastic deformation, i.e., the generation and motion of dislocations in the lattice structure. Conrad (2000) proposed that the electron wind, i.e., the force that is produced by electrons scattering off barriers in the electrical path, provides an additional force on dislocations to aid motion. Alternatively, Roylance (2001) proposed that an increased rate of diffusion and energy state of the material was produced by the electrical energy during EAF thus allowing easier dislocation motion. Regardless of the specific theory, the underlying principle is that the electrical energy aids the generation, arrangement (Yao et al., 1996), and motion of dislocations in the lattice structure during EAF.

Similarly Jones and Mears (2010) proposed three hypothetical factors that contribute to the effects of EAF. One is that the flowing electrons interact with flaws, both stationary (i.e., grain boundaries, voids, cracks, etc.) and moving (i.e., dislocations) within the lattice. This would cause localized resistive heating as well as a global temperature rise. The internal localized resistive heating at the microstructural level is far higher than the global temperature at the macroscopic view. This localized increase in temperature causes the lattice to expand around flaws and allow for dislocations to pass easier. Secondly the addition of electricity can impose a force on the dislocations as they flow through the material. This force is imposed as the flowing electrons impact a dislocation line moving through the material and therefore reduce the net forming force. Finally, the extra abundance of electrons caused by the application of electrical current, decreases the bonding forces between the ion cores.

Siopis and Kinsey (2010) found that at current densities of 250$[\frac{A}{mm^2}]$ the flow stress could be reduced by up to 30% for the compression of CuZn30 cylindrical specimens. Also, higher stress reductions were observed for fine grain structures during EA compression of Cu101 (See Figure 5). This plot compares the flow stress for a non-EA test to one at a current density of 250$[\frac{A}{mm^2}]$. Similarly Dzialo et al. (2011) found that the flow stress reduction was largest for specimens with higher Zn content (i.e., 35% compared to 30% and 13.5%) for tests with 120$[\frac{A}{mm^2}]$. These research efforts support the mentioned theories that the electrical current imparted enough energy to dislocations to overcome lattice obstacles (i.e., grain boundaries and impurity elements) which inhibit dislocation motion. That is the finer grain structured and higher Zn content specimens would be affected more by electrical current as they would have more lattice obstacles the dislocations are able to overcome.

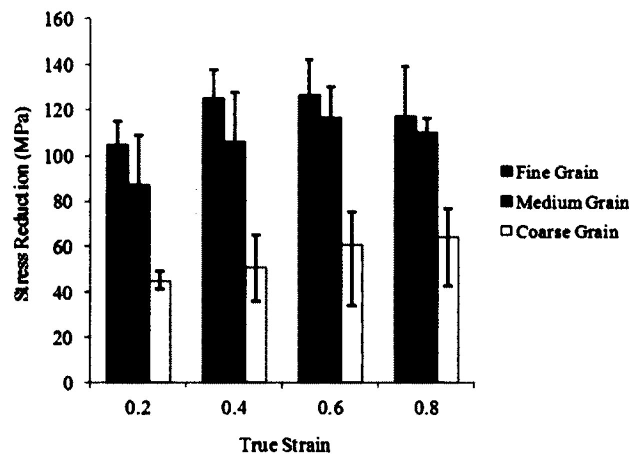

Figure 5: Reduction in flow stress at various strains and grain sizes. (Siopis et al., 2010)

1.5 Research Goals

A main goal for this research is to eliminate the effect of grain structure on strain gradients with the application of electrical current. Additional goals include to assess the

effects on the mechanical response of the material and to measure the temperature during EA forming to compare with conventional hot working parameters. Past research is revisited with the new capability for temperature measurement to investigate if the observed effects in past EAF results are simply due to differences in the temperatures achieved from resistive heating for the various specimen types or due to an electroplastic effect.

1.6 Summary

In this thesis, 3-point bending experiments of CuZn30 were conducted with both EA and non-EA processes. Digital imaging correlation (DIC) with a microscope system was used to measure strain gradients through the thickness of the specimens. Compared to the traditional, non-EA process, the strain gradients were nearly identical for various grain structures which would lead to consistent springback results as the elastic recovery would be similar. As expected, for both processes, the force reduction decreased with increasing grain size due to the Hall-Petch effect. Also, temperature was measured during the process. This knowledge is essential in order to understand the resistive heating induced. Finally, force displacement data was obtained to consider trends observed.

In addition, axi-symmetric EAF tests of commercially pure copper and three brass alloys were conducted to determine the temperature induced during EAF. This data was necessary to further asses past EAF compression test data (Dzialo et al., 2011). Results show that the EAF effects observed cannot be explained by initial temperature effects alone.

CHAPTER 2

THREE POINT MICRO BENDING

2.1 Experimental Methods

2.1.1 Loading Stage & Analog Transducers

The 3-point microbending experiments were performed on the 4448[N] (1000[lb]) loading stage shown in Figure 6. Displacement measurements were obtained with a Vishay Micro-Measurements Linear Displacement Sensor (LDS) HS25 with a fully active 350-ohm strain gauge bridge. The bending force was measured using a 111.2[N] (25[lb]) Sensotec precision miniature load cell with an accuracy of ± 0.13 at full scale. Both sensors were excited by 10[V] DC from an Elenco regulated power supply, model XP-575.

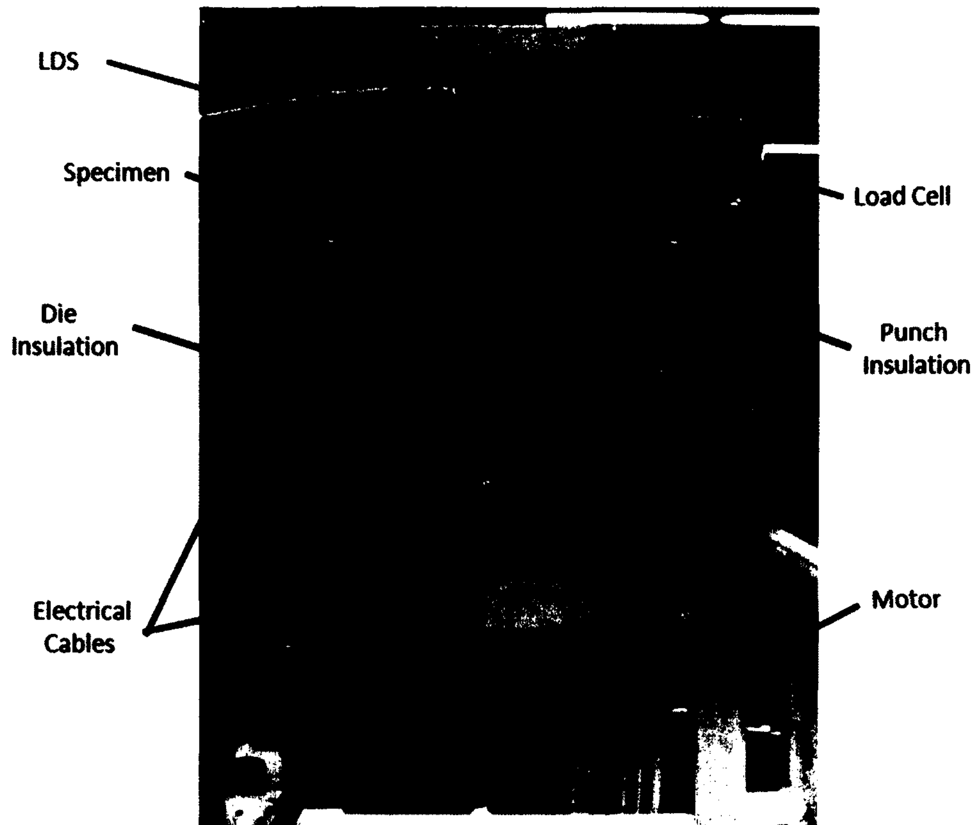

Figure 6: Loading stage used in experimental set-up

2.1.2 Current Supply

The electrical current for the EA process was provided by a 200[A], DC Lambda power supply. Due to melting and welding of the specimen to the die at this full capacity value, a constant current of 100[A] was applied to the specimens during the EA process. Thus, the current density applied was approximately 40[A/mm^2] for the 0.5[mm] thick, 5[mm] wide specimens. This current density did produce variations in results during past compression tests (Siopis et al., 2010). The current outputted from the power supply was within ±0.25[A] of the 100[A] desired value. Note that a 20[N] preload was applied to the specimens to ensure good electrical contact between the specimens and the dies before applying the electrical current.

2.1.3 Tooling

The dimensions for all of the tooling were based on the thickness of the specimen as per past research efforts. A diagram showing the tooling parameters is shown in Figure 7. The width of the die opening L_d is $7t$ (3.5[mm]) while the radius of the punch (R_p) and the die (R_d) radii are $1.5t$ (0.75[mm]).

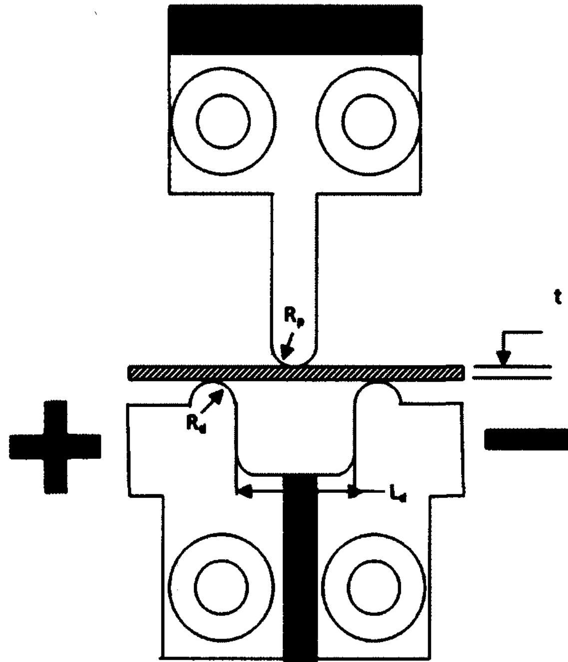

Figure 7: Diagram of tooling parameters

Note that the electrical current entered the left die, passed through the specimen, and exited out of the right die to complete the circuit. Therefore the electrons would be moving in an opposite direction with respect to the current. To electrically isolate the process, the two steel dies were mounted to a machinable ceramic while the punch and the die were wrapped in Kapton tape and the punch was secured to the upper platen with glass reinforced nylon bolts (regular hardware was used on the lower platen as the ceramic holder provided the electrical insulation). With the specimen electrically insulated, using DC current and based on the thin size of the specimen, the electrical

current could be safely assumed to travel uniformly through the specimen (no electrical skin effects). The punch was removed from the driving screws of the SEM stage and secured so to remain stationary during deformation. This was to keep the deformation around the punch in one location to prevent the deformation of interest from moving out of the field of view of the optical equipment.

2.1.4 <u>Digital Imaging Correlation (DIC)</u>

To measure the strain gradient through the thickness of the specimens, the non-contact method of Digital Imaging Correlation (DIC) was used. This method tracks a pattern of strong contrast as the material deforms and then calculates the change in distance between speckles (i.e., the strain). To capture these images the stereomicroscope system shown in Figure 8 was used due to the small field of view in this microforming process.

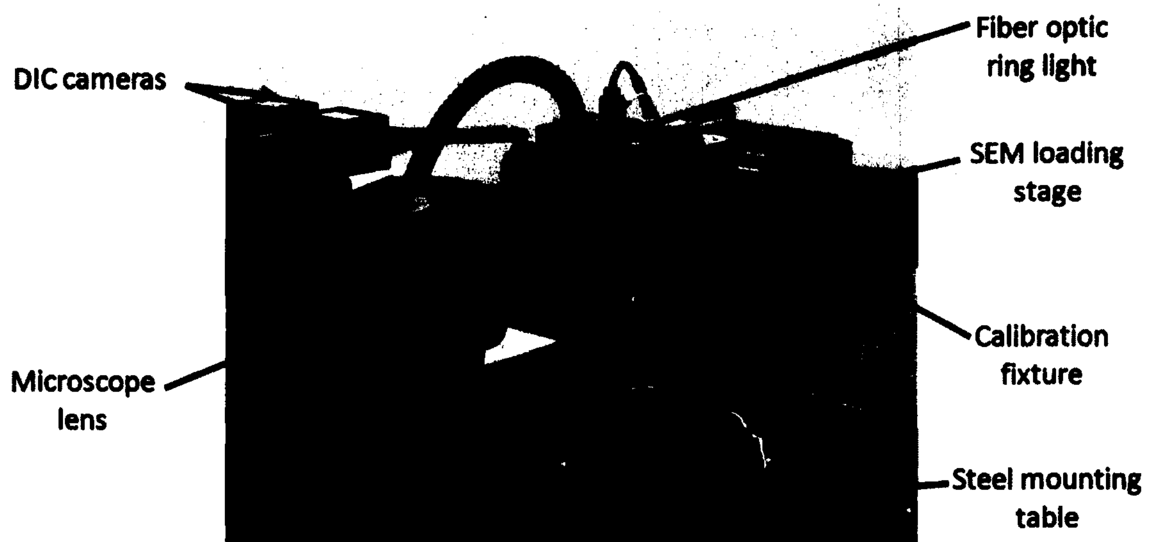

Figure 8: DIC stereomicroscope system.

The system contains two digital cameras which are set at angle of approximately 15 degrees. These two cameras work in a similar fashion to the human eyes by providing

depth perception. This allows the cameras to detect and measure out-of-plane motion as well as in-plane motion. Important specifications of the DIC stereomicroscope system are provided in Table 1.

Table 1: DIC stereomicroscope specifications.

Parameter	Value
Field of View	0.8 [mm] - 7 [mm]
In-plane displacement resolution	±60 [nm]
Out-of plane displacement resolution	±120 [nm]
Strain resolution	± 0.015
Stage movement	3 axis

For the tests preformed, the zoom setting was set to 2 which allowed for a pixel size of 1.22[μm] and thus 410 pixels through the thickness. This is over twice the resolution that could be achieved with the setup used in Wang et al. (2011)

Two different sets of images were required to calibrate the system. First a calibration is required to correct for distortions in the image caused by the complicated optical path and high magnification lenses. Note that this calibration is unique for the stereomicroscope system. To correct for distortions, the E pattern on the flat speckle pattern target (P/N CSI-016-D13 from Correlated Solutions Inc) was used to take a sequence of images containing in-plane motion. The standard parameters of a subset of 25 and a step of 5 were used for the distortion calibration. Secondly, 10-20 pairs of images were taken of in- and out-of-plane orientations of the pattern D on the grid stereomicroscope calibration target (P/N CSI-016-D12) to calibrate the stereo angle of the microscope system. All of the calibration targets are made of a sodalime glass with a fragile etched coating containing either the speckle or grid patterns. The etched coating must be facing the lens of the stereomicroscope when calibrating. For more detailed

information about calibrating the stereomicroscope system please refer to Correlated Solutions Application note AN-504.

Once the tests and the DIC image pairs were obtained from the tests, they were loaded into Correlated Solution's software VIC-3D. After the calibration was loaded an Area of Interest (AOI) was defined around the specimen (see Figure 9).

Figure 9: Example Area of Interest with subset size of 71.

Note that edges of the AOI are defined significantly above and below the specimen to allow the subset to capture the data at the edges. A subset size of 71 and step size of 3 were used in the DIC analyses based on past research (Wang et al., 2011) and was confirmed experimentally to be appropriate for this application. Note that DIC measures the strain on the side surface of the specimen as it is tracking the speckle pattern applied on that side surface. Note that the specimens were designed to have plane strain throughout the specimen (i.e., width ten times greater than the thickness).

2.1.5 Thermal Imaging

To measure the temperature of the specimen a FLIR SC 600 series thermal imaging camera was used on the opposite side of the specimen compared to the DIC system. To obtain approximately 10 points of temperature data through the thickness, a Close-up IR 2.9X Lens was attached to the thermal imaging camera, resulting in a pixel size of 50[μm]. To get accurate temperature readings the camera must be focused on an area with a known emissivity. Therefore, the specimen had to be covered with an enamel as the emissivity and reflective nature of the bar metal would cause inaccurate temperature readings.

2.1.6 Initiating Data Recording Using Triggering Ports

The voltage and current signals were outputted from the Lambda power supply via the J1 connector terminal on the backside of the power supply. A diagram of the connector is shown in Figure 10.

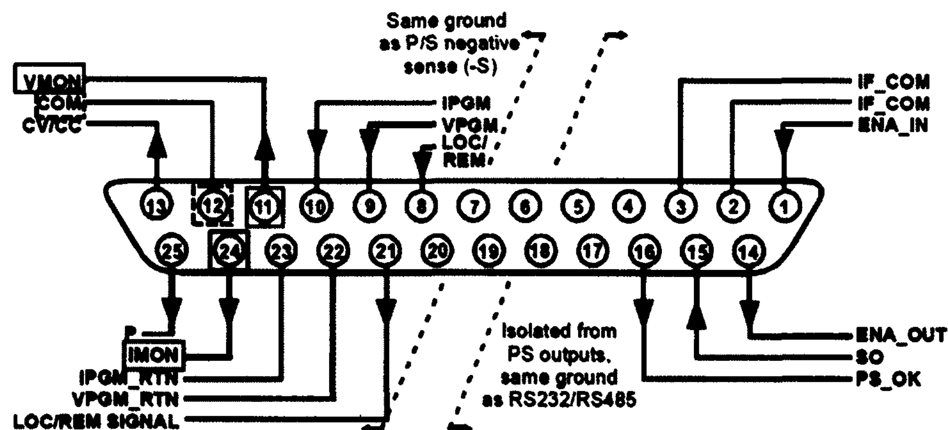

Figure 10: Diagram of J1 connector terminals for analog output from power supply. Voltage signal (VMON) highlighted in red and current signal (IMON) highlighted in green.

Note that pin 12 (COM or common) is the return for both the voltage (pin 11, VMON or voltage monitor) and current (pin24, IMON) signals. Both the voltage and current signals

are 0 to 5[V] proportional to the minimum and maximum the power supply can output. For example, if the unit was supplying 100[A] of current, the current signal (IMON) would read 2.5[V]. The voltage and current signals (along with the load cell and Linear Displacement Sensor signals) were connected to a NI-USB-6259 DAQ as shown in Figure 11. Note that all signals were wired to be analog differential inputs.

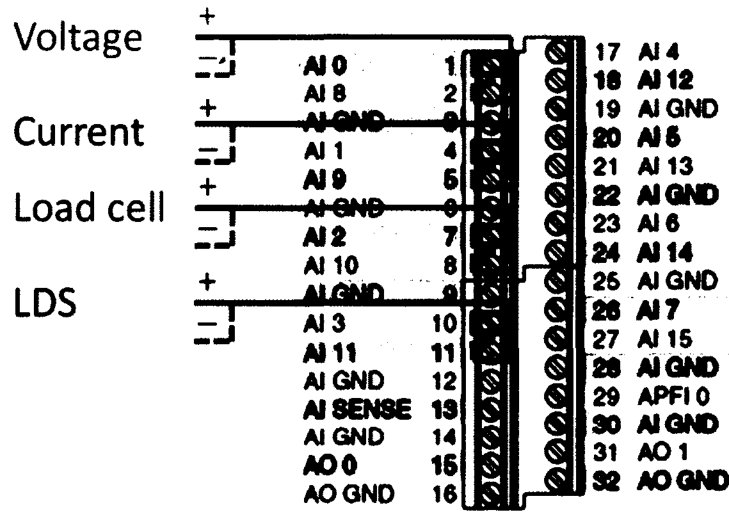

Figure 11: Analog inputs for NI-USB-6259 DAQ.

The NI-USB-6259 DAQ was also used to initiate the recording for the DIC and thermal images, as well as the analog signals by manually triggering. The NI-USB-6259 DAQ simply connects to a PC via a standard USB cord. To trigger the data collection as well as the DIC image recording (see Figure 12) the built in 5 [V] supply (pin 96) on the DAQ board was wired through a switch and then to the first digital input of the DAQ (pin 66).

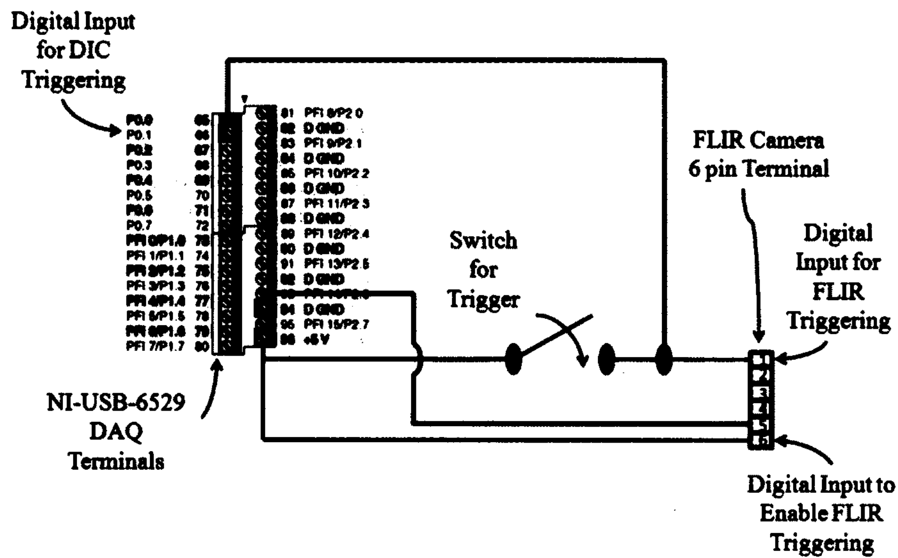

Figure 12: Wire diagram for DIC and FLIR triggering.

Similar wiring was used for the FLIR camera to be triggered at the same time as the DIC images. Another wire was connected from the trigger switch to pin 1 of the 6 screw pole terminal in the back of the FLIR camera. However, for triggering to be enabled, pin 6 had to be set high. The same 5[V] from the DAQ was used and pin 5 had to be used to ground the FLIR camera (see Figure 12).

With the wiring set, the triggering would need to be armed in the software programs for DIC and FLIR. The program used to record the DIC images, Vic-Snap 2010, was used to read in the analog data from the NI-USB-6259 DAQ (recall Figure 11) using the data acquisition command. Note that Vic-Snap was used instead of more conventional programs like Labview to read in the analog data because of its ability to record DIC images. Vic-Snap would record one point of data from each of the signals every time a pair of DIC images was taken. To reduce the effects of signal noise, oversampling of 500 samples was used (i.e., 500 data points were obtained and the average data point was recorded). To enable the VIC-Snap program for triggering, The TTL image option was used to start the recording when a digital input (recall PO1 on the

NI board in Figure 12) was driven high and continued recording as long as the input remained high. To arm the FLIR camera, ExaminIR MAX was used. Under record conditions, the camera was set to start recording when digital input 1 was driven high. ExaminIR would start recording when triggered, but unlike Vic-Snap it wouldn't stop when the trigger switch was opened again. Therefore, recording would be stopped manually after the test was complete. A max recording time of 90[sec] was used to avoid accidentally creating an overly large data file. Both Vic-Snap and ExaminIR were set to record at the same rate of 2[Hz] (1 sample/image every 500[ms]).

2.1.7 Specimen Preparation

The specimens were 0.5mm thick sheets of CuZn30 with a width of 5mm to ensure a plane strain condition. All the specimens were heat treated in a Lindberg-Blue tube furnace under a pure argon gas environment to prevent oxidation. Time and temperature from previous research was used to obtain specimens with coarse, medium and fine grain structures, corresponding to approximately 2-4, 10-15, and 25-30 grains through the thickness respectively (Wang et al., 2011). See Table 2 for these parameters.

Table 2: Heat treatment parameters with a duration of 60 [min].

Grain structure	Temperature [°C]	Grain size [μm]	Standard deviation [μm]
Fine	400	17.2	1.47
Medium	500	35.5	2.96
Coarse	665	142.9	12.33

Because theoretically the specimen will only contact the die along a tangent line of the die's radius, the surface finish at the specimen/die interface is critical to the electrical connection for the experiment (with a rougher surface leading to worse electrical contact). Therefore, after the heat treatment of each specimen the surface that would

contact the dies was sanded with 600 grit sandpaper. This is done to ensure that each specimen would have a consistent surface finish at the specimen/die interface even across grain structures. Table 3 shows the surface roughness data from a Mitutoyo Surftest SJ-400 profilometer that was used to verify the sanding effect on the specimens.

Table 3: Surface roughness of specimens with various grain structures.

Grain structure	Ra [μm]
Fine	0.15
Medium	0.23
Coarse	0.33
Coarse (Sanded)	0.20

The through thickness surfaces of the specimen that would later face optical equipment (i.e., the longer edges of the specimen) were also sanded with a 400 grit sandpaper. This sanding was to roughen the surface which aids the bonding of high heat enamel to the specimen. This was necessary because standard spray paint on an untreated surface was prone to failing (cracking, chipping or pealing off the specimen) at the high strain values at the end of the tests. The entire specimen was then cleaned in acetone after sanding.

For the through thickness surface facing the FLIR camera, a white, high heat enamel was applied to give the through thickness surface a known emissivity for the temperature measurements. For the through thickness surface facing the DIC system, the same white high heat enamel was also applied. However, while the enamel was still wet, carbon toner, from a used printer cartage, was "flicked" onto the specimen with a small, stiff brush. The enamel then dries and the carbon toner speckles are secured to the enamel, thus creating the speckle pattern that was tracked for DIC. Generally, there should be 3-5 pixels through each speckle. An example of good speckle pattern is shown in Figure 9.

2.1.8 Testing Procedure

First, the fully prepared specimen was placed on the dies with the speckle patterned surface facing the DIC stereomicroscope system. To ensure the specimen is not misaligned with respect to the die, the side facing the FLIR camera was pushed against a machined block that was held against the die. Once the position of the specimen was set a 20[N] preload was applied to the specimen. This preload ensured an adequate electrical contact was created to complete the electrical circuit. Note that even though no electrical current was passed through the non-EA tests, the preload was still applied to be consistent between processes. Once the preload was applied, the supply that controls the speed of the SEM stage was set to 60% of the full scale (approximately $0.8[\frac{mm}{sec}]$). Faster speeds may result in blurred DIC images. Once the DIC system and FLIR camera were in focus, the trigger was switched on to start recording the data. If the test was an EA process test, then the current was applied immediately after setting off the trigger. After one or two frames of data are recorded the motor controlling the SEM stage was turned on to begin forming the specimen. Finally after the specimen was deformed 7t (3.5[mm]) the SEM stage was turned off. If the current supply was on, then that was stopped as well. Finally, the trigger was switched off to stop data recording and the thermal imaging was stopped.

2.2 Results

2.2.1 Strain Results

An example of the strain distribution data from one of the tests is shown in Figure 13. The line directly under the punch is where the strain values were extracted from the software to determine the strain gradient through the thickness. Note that while the exact center under the punch may not have been exactly identified, the strain distribution to the right and left of the line was consistent as shown in Figure 13. Therefore this error is negligible. Also note that the image shown in Figure 13 was taken with one of the two DIC cameras in the stereomicroscope system. Recall that the cameras are set at a stereo angle and therefore are not perpendicular to the specimen. This is why the punch does not appear to be in the center of the specimen being bent.

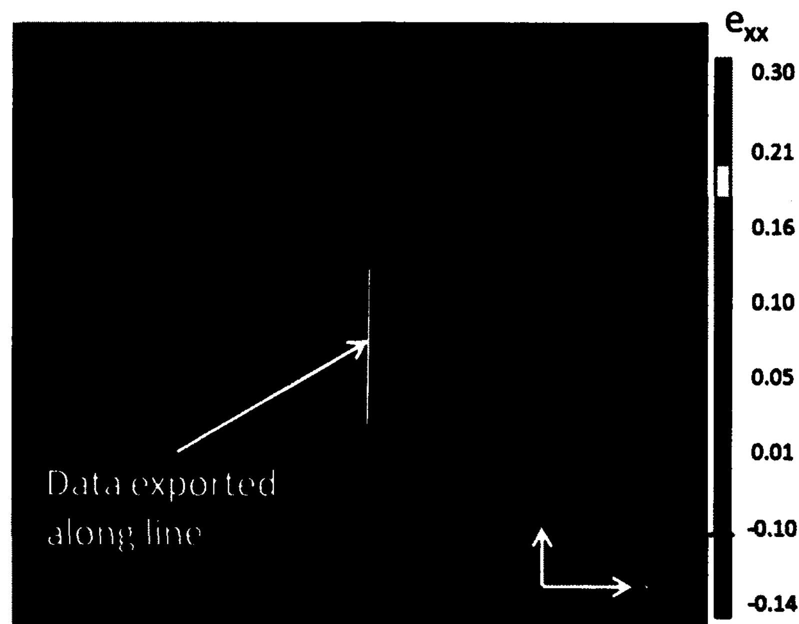

Figure 13: Strain distribution data from DIC analysis.

The strain shown is the strain on the side surface of the specimen. Recall that the specimens where designed for plane strain; therefore, the strain at the surface should

represent the strain throughout the specimen. The strain data was exported as Lagrangian strain e_{lag} and was then converted to engineering strain using:

$$e_{eng} = \sqrt{2(e_{lag} - 1) + 1}\,, \tag{1}$$

where e_{eng} is the engineering strain. The average strain distribution (of the fiver specimens formed) through the thickness of the specimens formed without any electrical assistance is shown in Figure 14a for the varying grain structures. Note that the error bars shown in this figure and all others in this thesis are the maximum and minimum values for the five tests conducted.

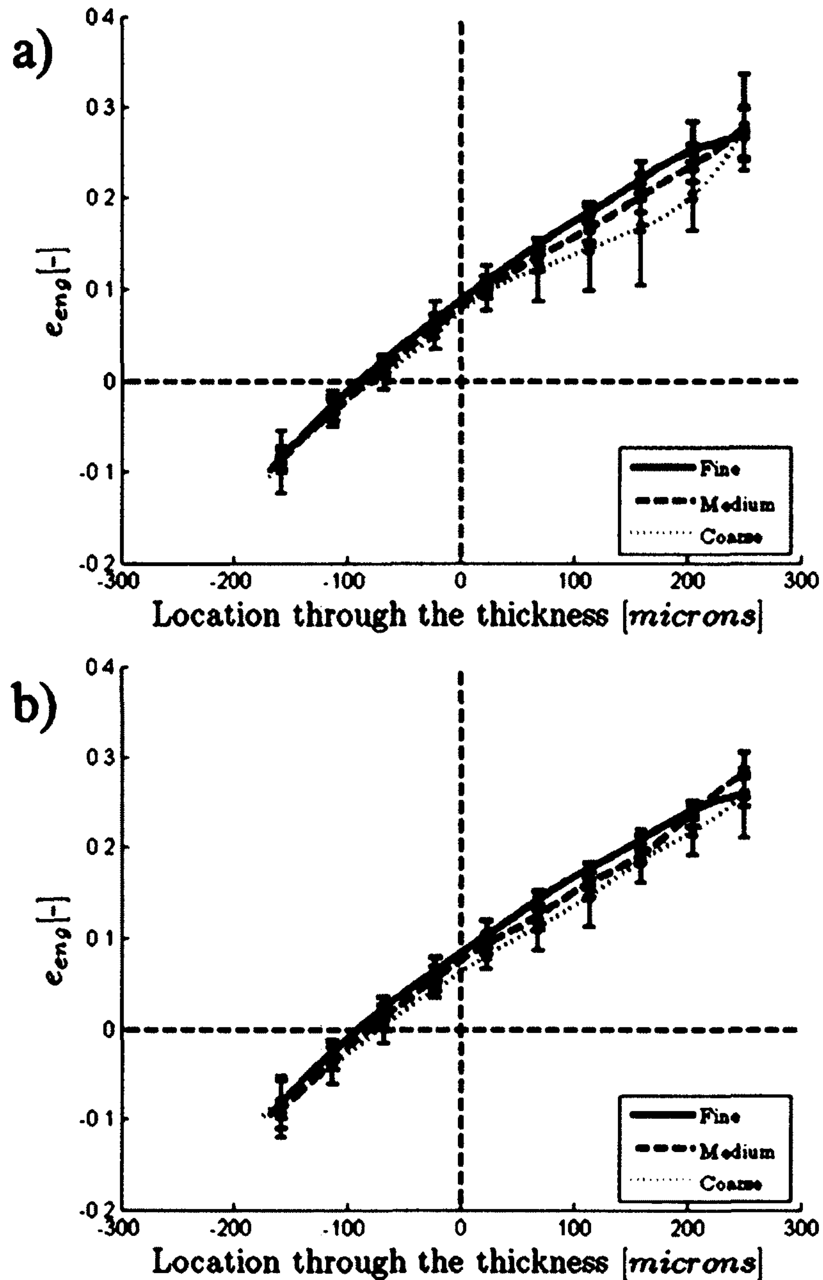

Figure 14: Strain distribution under the punch for different grain structures for the a) non-EA and b) EA processes.

The zero location through the thickness corresponds to the center of the specimen with negative and positive location values corresponding to the compressive and tensile sides respectively. Note that a positive strain value exists at the center of the specimen indicating that the neutral axis (i.e., zero strain location) shifted towards the compressive

side during this microbending process. The strain gradients on the compressive side of the specimens were similar for the three grain structures; however, on the tensile side lower strain gradients exist for the coarser grain structures (i.e., a maximum strain value variation of 0.11 at 159 microns for the fine versus coarse specimens). Note though that this variation was within the error bars for the data at this location. The coarse grain structure yielded the highest error bar range where the fine grain structure produced the least. Note that there is some data loss on the compressive side of the specimen. These results are similar to that found in (Wang et al., 2011) (See Figure 2). However, the previous data showed a variation in the strain gradient across the entire thickness as opposed to only the tensile side. Note that strain values closer to the surface were able to be obtained due to the doubling of magnification with the inclusion of the stereomicroscope system.

The average strain distribution through the thickness for the EA specimens is shown in Figure 14b for the varying grain structures. As with the non-EA specimens, the neutral axis shifted during the microbending process. The trend of higher variation with the coarser grain structures was also observed with the EA specimens; however, the variation was significantly lower for the EA process (especially on the tensile side of the specimen). Compared to the non-EA specimens, the strain gradient was less affected by the grain structure for these tests. The tensile strain at the surface, for all specimen types was comparable (see the 250 [micron] location) despite the change in strain gradient elsewhere. This is expected as strain at the surface is a geometric parameter determined to be 0.25 [-] by

$$\varepsilon = \frac{\Delta l}{l} = \frac{(R+t)-\left(R+\frac{t}{2}\right)}{\left(R+\frac{t}{2}\right)} = \frac{\frac{t}{2}}{R+\frac{t}{2}} = \frac{\frac{t}{2}}{1.5t+\frac{t}{2}} \tag{2}$$

The strain distribution for individual grain structure tests, with and without current application, is shown in Figure 15.

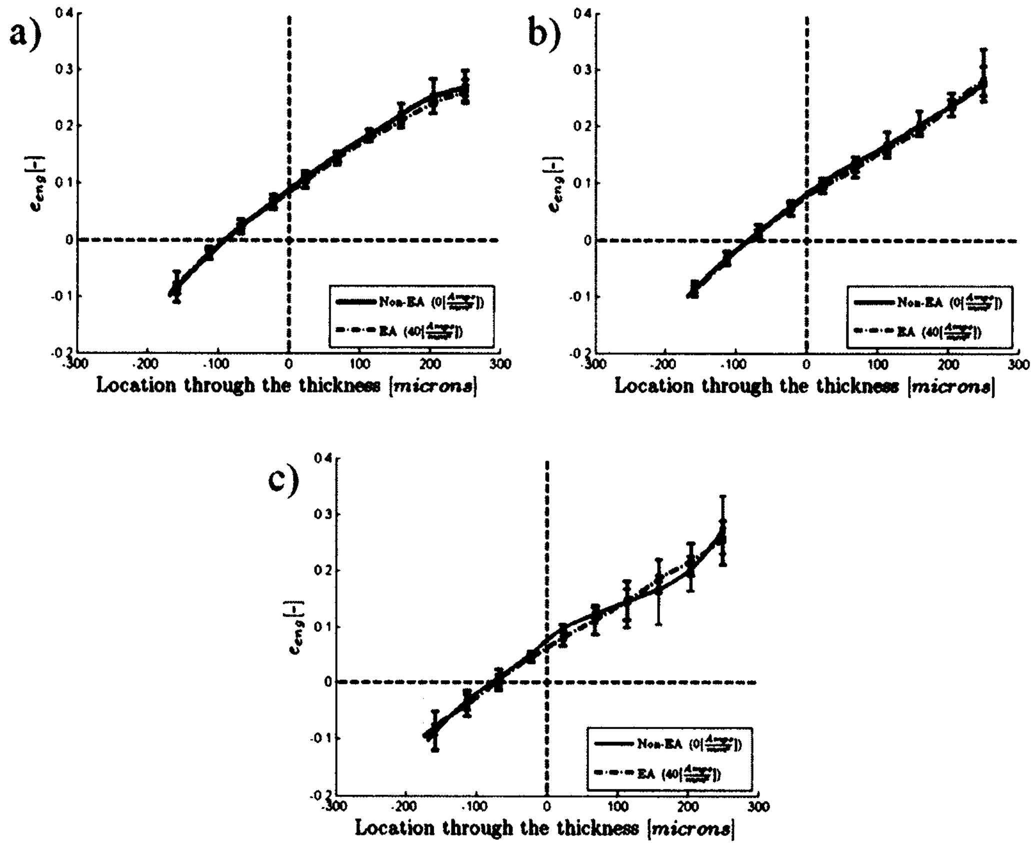

Figure 15: Strain distribution under the punch for a) fine b) medium and c) coarse grain structures

The application of current had a very small effect on the strain gradient for the fine grain structure tests (see Figure 15a); however, error bars are less for the EA tests. The strains are almost identical on the compressive side of the specimen and only after 100 microns from the center does some deviation occur. As with the fine grain structure, the strain gradients for the medium structures (see Figure 15b) are very similar. Finally, the strain gradient for the coarse grain structure tests (see Figure 15c.) showed the largest effect to the application of electrical current. The strain gradient for the EA tests was more linear than the non-EA tests and the consistency improved considerably.

2.2.2 Force Results

In addition to the strain gradients through the thickness, the difference between the force-displacement data for the non-EA and EA processes was investigated. The average measured forces for the fine and medium grain structure tests are shown in Figure 16a and Figure 16b respectively. The trajectory of the non-EA microbending process is as to be expected for a bending process with continuously increasing force values with displacement that plateau and decrease towards the end of the process.

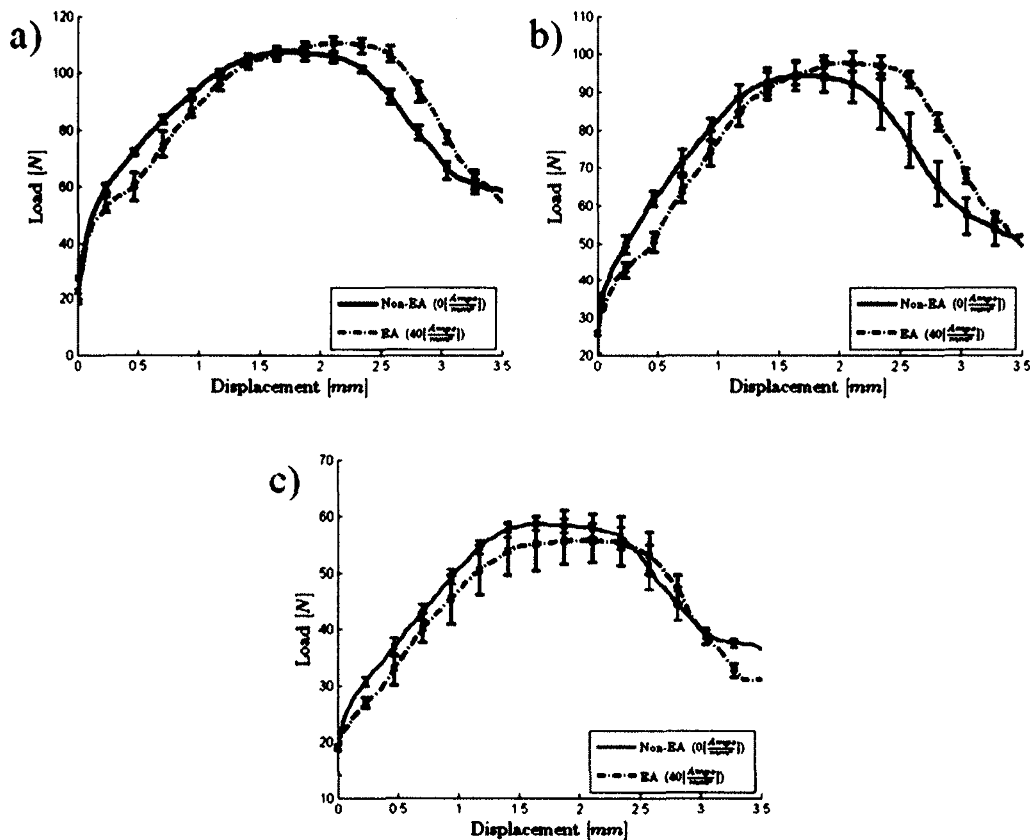

Figure 16: Measured force for a) fine b) medium and c) coarse grain strucures

The trajectory of the EA process is different for the fine and medium grain structure cases. Initially the loading follows a similar slope to the non-EA process. However, from approximately 0.1 to 0.5[mm] of displacement, the force value increases significantly less with displacement than what was observed for the non-EA process. As

will be shown shortly, this is due to thermal effects. After 0.5[mm], the force values again increase and follow a similar trend to the non-EA process with less force required until the curves intersect at approximately 1.5[mm] of displacement. After about 1.6[mm] of displacement, the average force from the EA process increases and plateaus at a maximum value slightly higher (i.e., only 3.2% higher) than the non-EA process. Towards the end of the tests (past 3[mm] of displacement) the average force for the EA process continues to decrease with a similar slope while the average force for the non-EA process begins to plateau again. The cause of this behavior is the varying force at the die/specimen interface that affects the electrical connection as will be shown in subsequent temperature data.

The average measured force for the coarse grain structure tests (shown in Figure 16c) has a slightly different trend. For these tests, the application of current had a much smaller effect than the other grain structures, which is consistent with data from Siopis and Kinsey (2010). As with the other grain structures, the force values from the EA process did show a reduction of force in the beginning of the test (<0.5[mm]); however, the force reduction was much less pronounced than the other two grain structures. Also, the peak force observed for the EA process did not exceed the peak force from the non-EA process. Also unlike the other two grain structures, the force from the EA process plateaued out at the end of the test (after about 3.25[mm] of displacement, similar to the non-EA process, but at a lower value.

The measured force for all grain structures from the non-EA process can be seen in Figure 17a. Note that these curves have a similar peak force value around approximately 1.75[mm] of displacement. As expected from the Hall-Petch effect, the

maximum force decreases as the grain size increases due to fewer grain boundaries for dislocation pile-up. Results typically vary more for coarse grain structures since the properties and orientation of individual grains have a significant effect on the overall material behavior. However, for this data set, this effect was not observed.

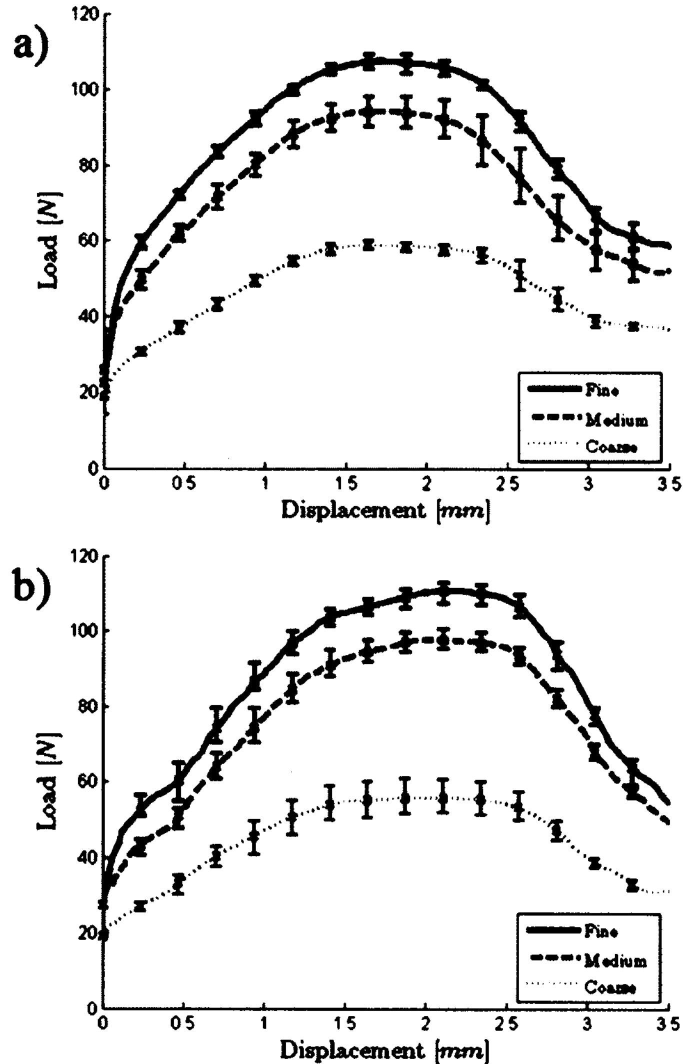

Figure 17: Measured force for all grain structures during a) non-EA and b) EA tests.

The measured force for all grain structures from the EA process is shown in Figure 17b. For all the grain structures from the EA process, the force values start to decrease at a displacement of about 2.5[mm]. The peak force value for the fine and

medium cases occurs at approximately 2.2[mm]. The displacement where the force increases at a steeper rate (around 0.5[mm]) was consistent for all grain structures.

2.2.3 Temperature Results

To export the temperature data recorded from the FLIR camera an Area of Interest (AOI), shown in Figure 18, was defined under the punch. All of the data points within AOI are considered to obtain an average temperature value. The size and location of the AOI shown in Figure 18 was chosen for two main reasons. First, unlike the DIC software, the IR examiner software cannot track a moving/deforming AOI. Because the punch is stationary during the test, an AOI under the punch will include only the specimen even as it deforms. The second main reason was that this location is where the strain gradients were exported from and is in-line with the load cell which is measuring the force data. The variation of the data in the AOI was approximately 80 which is 21% of the values measured. Note that the thermal imaging shows no electrical current passing through the punch.

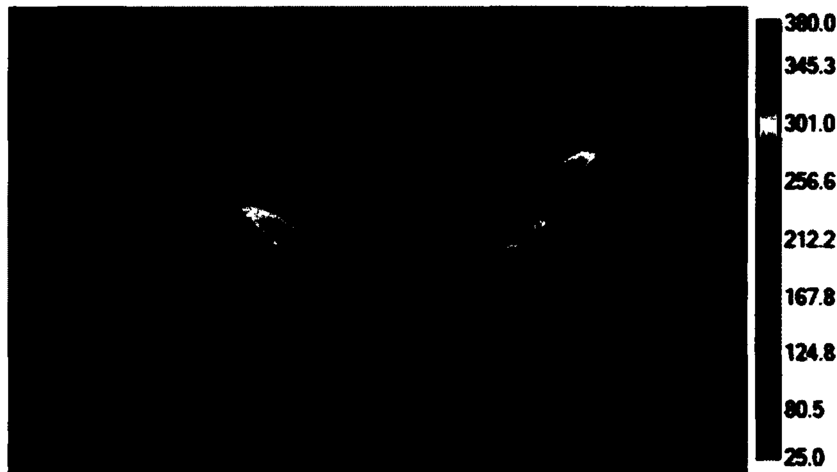

Figure 18: Area if interest defined under punch to export temperature data.

Figure 19a shows the average temperature under the punch (along with the force data) for the EA fine grain structure tests. For the first 0.5[mm] of displacement, the temperature spikes to the highest value seen throughout the test. Such initial spikes in temperature have been observed by other researches during EA bending as well (Salandro et al., 2010). The period where the force didn't increase significantly (i.e., from 0.1 to 0.5[mm]) is also when the maximum temperature was observed. After the initial temperature spike, the temperature plateaus to a consistent value of approximately 100[°C] until 3[mm], where the temperature starts to rise again until the end of the tests. Despite forming at an elevated temperature of 100[°C] and above, the peak force from the EA tests exceeded the peak force from the non-EA tests. Note that a significant change in yield strength is not expected for Cu 260 until temperatures exceed 300[°C] (Cubberly et al., 1978).

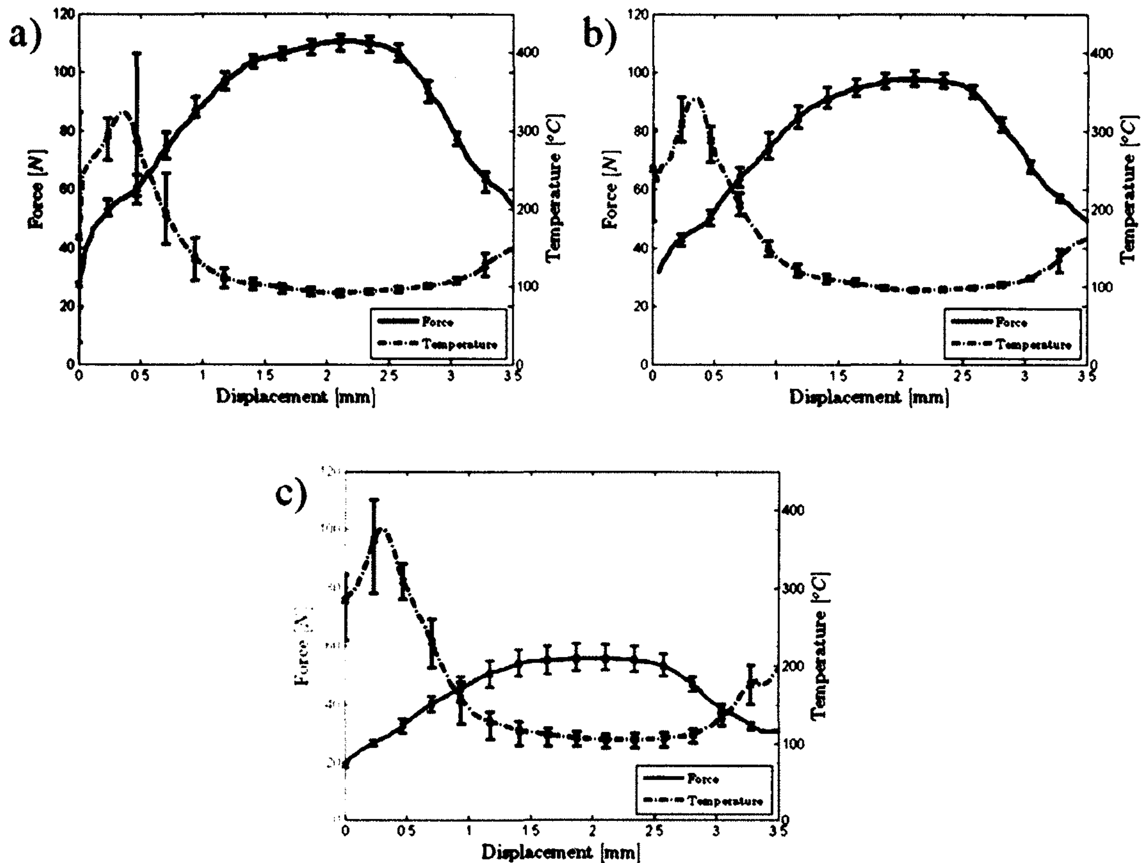

Figure 19: Measured temperature and force for a) fine b) medium and c) coarse grain structures from the electrical-assisted process

The same trends were observed for the medium and coarse grain structure tests from the EA process as shown in Figure 19b and Figure 19c, respectively. The coarse grain structure tests yielded the highest average temperature yet still had the least force reduction when compared to the other two grain structures. (Note though that the error bars overlap for these temperature measurements.) The relation between grain structures is better shown in Figure 20, where the temperature curves are plotted together. Others have observed similar temperature profiles with higher temperatures at the die contact compared to the center of the specimen (Salandro et al., 2011).

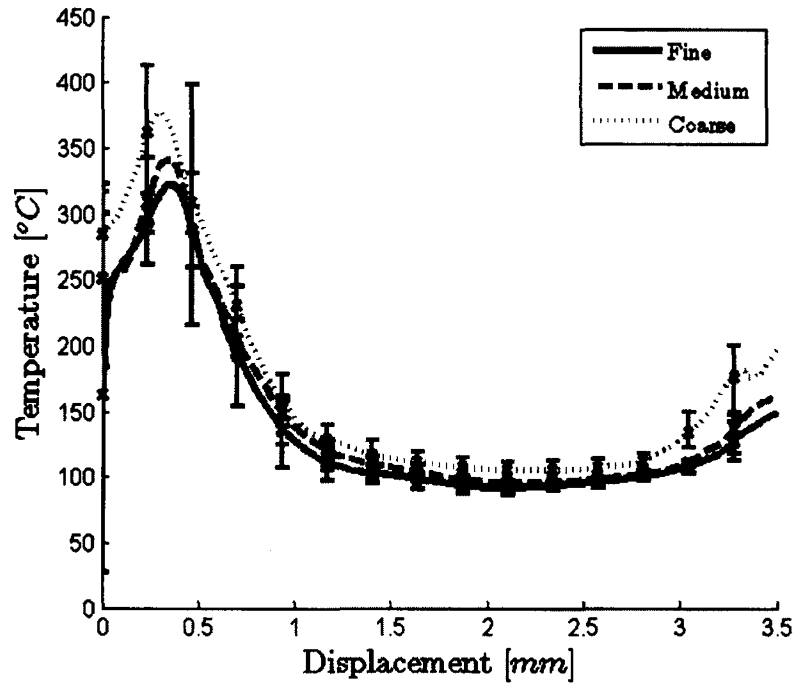

Figure 20: Average temperature under the punch for the electrical-assisted process

The temperature profile from one of the EA tests at key points in the temperature curve is shown in Figure 21. As is evident in this figure, the temperature profile is fairly uniform throughout the specimen at all of these key points. Thus considering the AOI data is acceptable. However, early in the tests, varying electrical contact provided inconsistent temperature results as will be shown in CHAPTER 4.

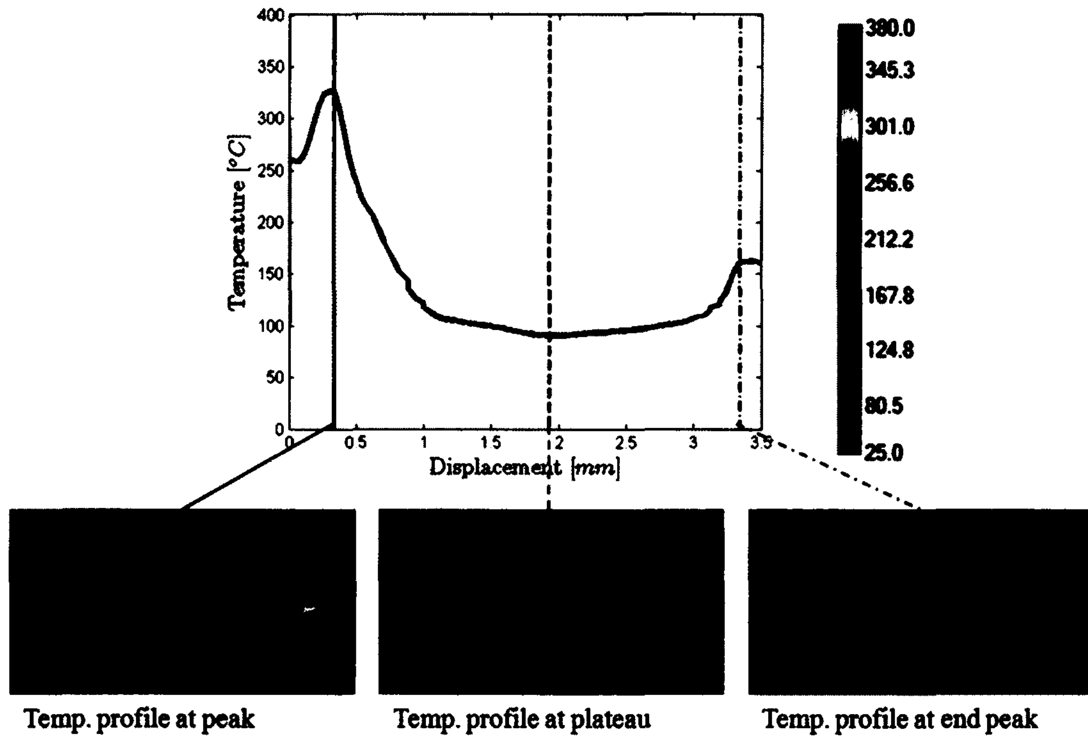

Figure 21: Temperature profiles at key points of the temperature curve.

Note that high deviations from the average are observed at the temperature spike in the beginning of the tests for all grain structures. This is likely due to varying electrical contact with grain structure. As shown in Figure 22 the temperature throughout the test was directly related to the voltage and thus the power being supplied to the specimen as the current was held constant at 100±0.25[A]. However, despite the coarse grain structure specimens producing the highest temperatures, the lowest amount of voltage to maintain 100[A] (see Figure 23) was required for this case. Slightly higher variations were also observed with the coarse grain structure specimens.

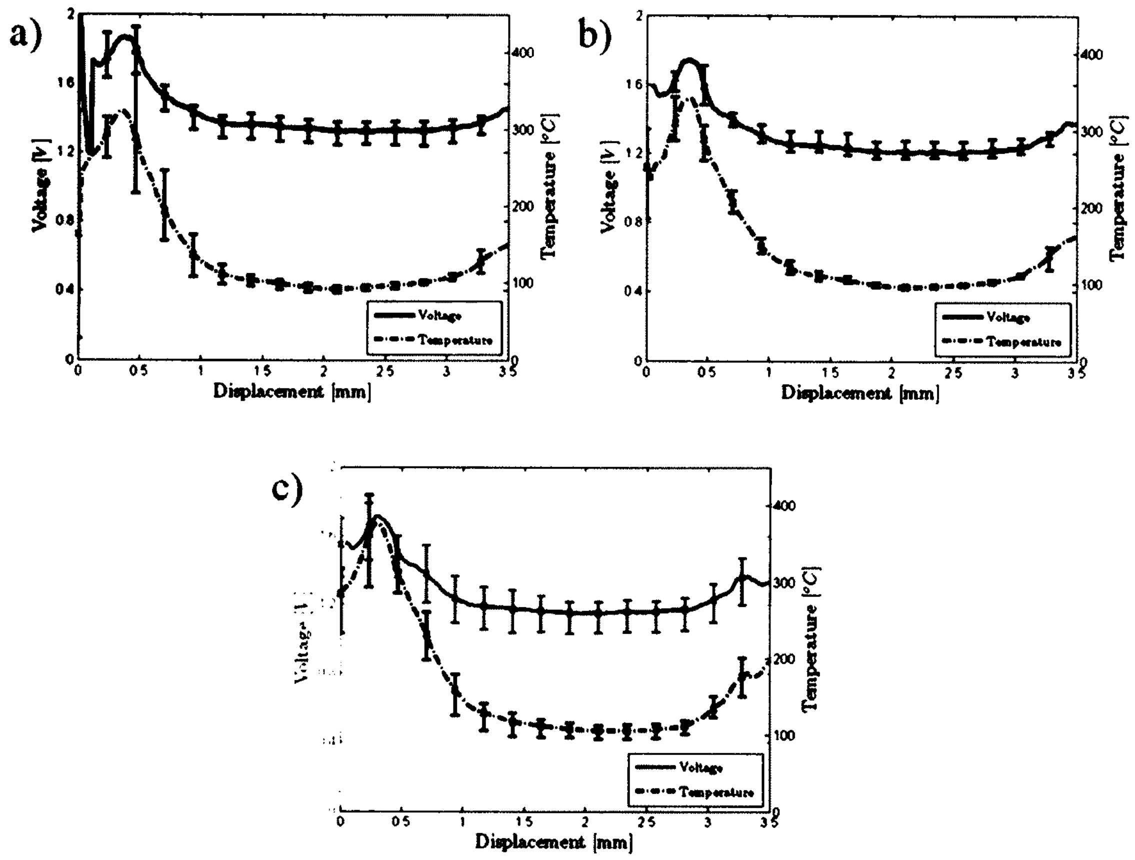

Figure 22: Measured temperature and voltage for a) fine b) medium and c) coarse grain structures from the electrical-assisted process

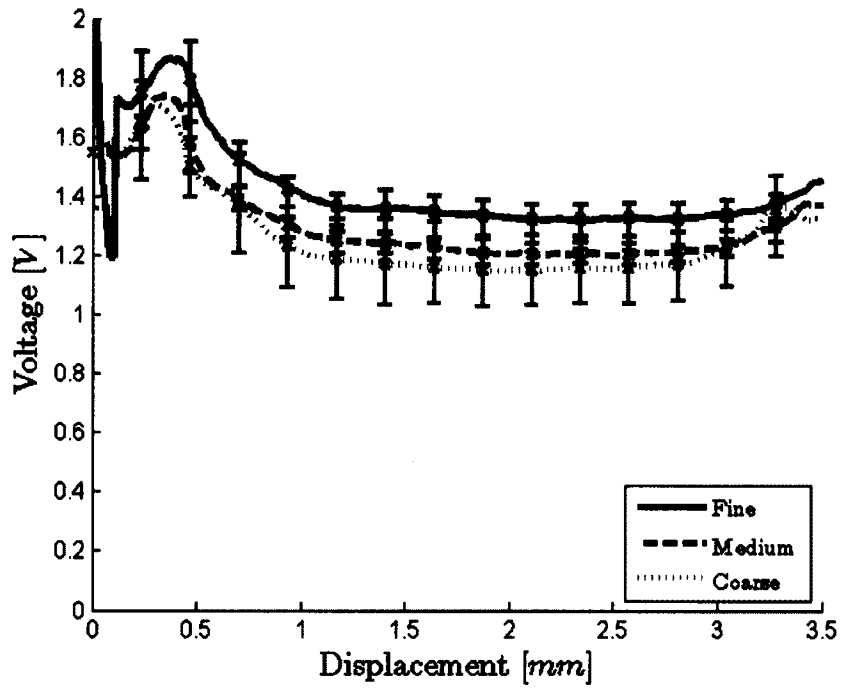

Figure 23: Average voltage for the electrical-assisted process

CHAPTER 3

COPPER WIRE TEMPERATURE TESTS

3.1 Copper Wire Test Motivation

In order to assess at least the initial temperature values for experiments in Dzialo et al. (2011) and Siopis and Kinsey (2010), axi-symmetric compression tests with current applied were conducted on commercially pure copper (Cu101, 99% Cu) and three brass alloys (Cu226, C260, and C270 with 13.5%, 30%, and 35% Zn respectively). However, only preloads were applied to determine the initial temperature without deformation.

3.2 Experimental Methods

3.2.1 Testing Equipment

The SEM stage was used again with the same load cell and LDS as specified in CHAPTER 2. The FLIR thermal imaging camera with the Close-up IR 2.9X Lens was again used to measure temperature. The tooling consists of upper and lower platens with flat die faces. Note that the same Lambda power supply was used to supply the current. The platens are insulated from the SEM stage with electrical grade fiberglass plates and attached to the loading stage via glass reinforced nylon bolts. A procedure very similar to the three point bending tests was used to trigger the data recording. Since no DIC images were obtained, a Labview program was used to record the analog signals from the NI-USB-6259 DAQ after manually triggering the test.

Figure 24: SEM stage with tooling for EA axi-symmetric compression.

3.2.2 Copper Wire Specimen Preparation

As with the three point bending specimens the commercially pure C101 wire specimens were heat treated in a Lindberg-Blue tube furnace under a pure argon gas environment (parameters shown in Table 4). The brass alloys were not heat treated since the as-received grain sizes for the varying Zn content materials were nearly identical (Dizalo et al., 2011).

Table 4: Heat treatment parameters for copper wire specimens.

Grain structure	Temperature [°C]	Duration [hrs]	Grain size [μm]
Fine	325	1	276.68
Medium	500	1	88.3
Coarse	1000	24	21.35

After heat treating, the specimens are sprayed with a high heat enamel. Recall this is to provide the FLIR with a surface of known emissivity. The ends of the specimens that will contact the platens were sanded to remove any enamel and to create a constant surface finish for electrical connections.

3.2.3 Copper Wire Testing Procedure

While holding the specimen straight and perpendicular at the center of the platen, a 30 [N] preload was applied to fix the location of the specimen and to assure electrical contact. Note that this preload will not plastically deform the specimen (i.e., only a 38.2 [MPa] stress compared to a 54 MPa yield strength for the lowest value of the material tested). Once the specimen was secured, the FLIR camera was focused on the surface of the specimen. The data recording was then triggered, and the current supplied to the specimen. After 90 seconds, the recording was stopped and the current shut off.

3.3 Results

As with the bending tests, an AOI was defined over the specimen. However, unlike the bending specimens, the copper wire specimens did not move so the AOI (shown in Figure 25) could be defined over the entire specimen. Again, all data points within the AOI are averaged.

Figure 25: Area of interest defined over copper wire specimen.

3.3.1 Heat Treated Copper

The temperature results for the heat treated commercially pure copper (C101) wire specimens at a current density of $120[\frac{A}{mm^2}]$ are shown in Figure 26. The coarse grain structure specimens yielded the highest temperatures. While the medium grain structure specimen yielded the lowest temperature at the same current density with the fine grain structure falling in between. For all grain structures an initial spike in the temperature was observed within the first 3 seconds of the test. After the first 10 seconds the temperature reached a more consistent value with a slight increase until the end of the tests.

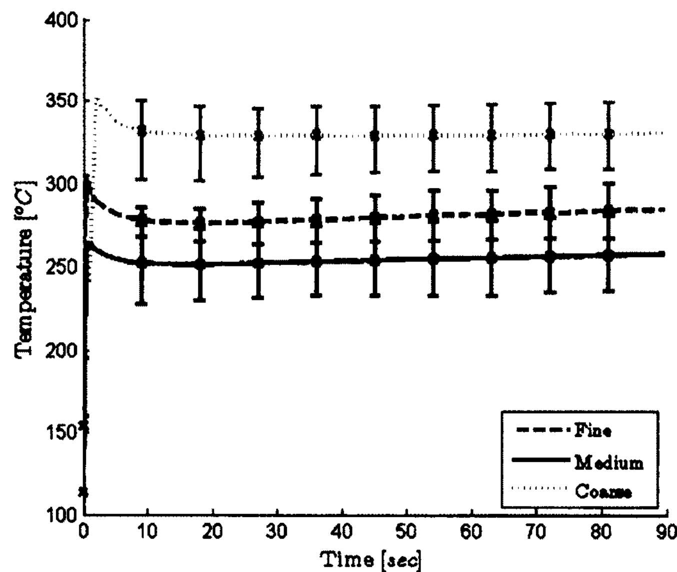

Figure 26: Temperature versus time for heat treated C101 at a current density of $120[\frac{A}{mm^2}]$.

Concerns with the heat treating may have prevented a consistent trend for a grain size versus temperature to be obtained. However for this simple assessment to consider past results, the higher temperature coarse grain structure results were sufficient. Since the coarse grain structure results in Siopis and Kinsey (2010) had the least flow stress reduction during EAF, based on these purely static results, this could not be explained by

temperature effects alone. Note while these tests did not include continuous deformation, the coarse specimens had the highest temperature initially and throughout the three point bending tests presented in CHAPTER 2.

3.3.2 Copper Alloys

The temperature results for the as-received Cu Zn alloys (i.e., 13.5%, 30% and 35% Zn content) at a current density of $120[\frac{A}{mm^2}]$ is show in Figure 27. As with the heat treated copper, a temperature spike was observed within the first 3 seconds of the test. The alloys with the higher Zn content yielded the highest average temperature. Note however that the variations between temperature for the three alloys was only approximately 30[°C]. A higher variance between tests for the specimens with lower Zn contents was also observed. As with the three point bending results these variations are likely due to inconsistent electrical connections.

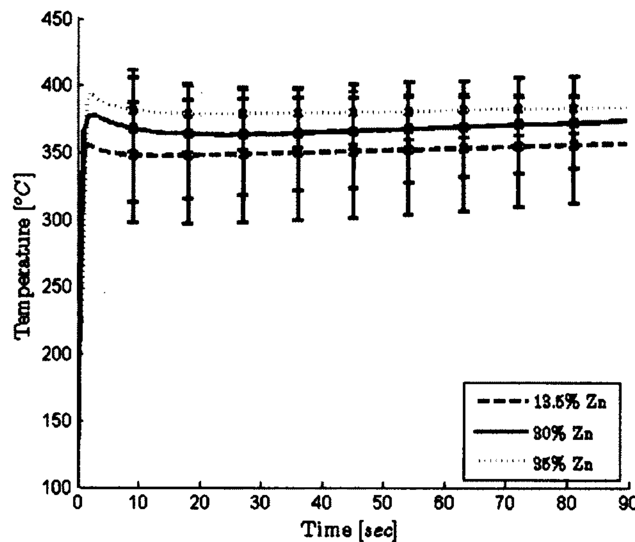

Figure 27: Temperature versus time for brass alloys for a current density of $120[\frac{A}{mm^2}]$.

CHAPTER 4

DISCUSSION

4.1.1 Strain Value at the Edge of Bending Specimens

Note that in Wang et al. (2011) a concern was that the varying strain gradients would cause different strain values at the surface. This was disconcerting since strain at this location is a geometrically driven value. With the microscope system being able to provide more accurate data especially close to the surfaces, the measured strain at the surface on the tensile side was the predicted value of 0.25[-] for all tests as in Equation (2). Thus, the strain gradients can vary with miniaturization while still being constant at the surface.

4.1.2 Initial Temperature Spike

In both the EA bending specimens and the copper wire temperature tests, an initial temperature spike was observed. This temperature spike is believed to be caused by the electrical contact between the specimen and the die or platen. The temperature spike was much more pronounced in the bending tests. This may be because the specimen is theoretically supposed to contact the die along a tangent line on the die radius. In contrast, the copper wire specimens will contact the platen across the entire circular surface of the specimen.

For both tests, the specimens with the coarser grain structure yielded the higher temperature spikes. Again, this may be due to electrical contact. Recall that heat treating the specimens roughened the surface (see Table 3) and a rougher surface leads to worse

electrical contact. Perhaps sanding the surface of the specimens was not sufficient for creating consistent electrical contact.

4.1.3 Relation Between Maximum Temperature Location and Voltage Sign

For the three point bending tests, the location of maximum temperature shifted within the temperature spike. An example of this can be seen in Figure 28 from one of the fine grain structure tests. The position of maximum temperature in the specimen was initially located near the die connected to the positive voltage lead. As the specimen deformed, the location of maximum temperature moved to the die connected to the negative voltage lead. After 2.5[sec] the temperature is more uniform throughout the specimen.

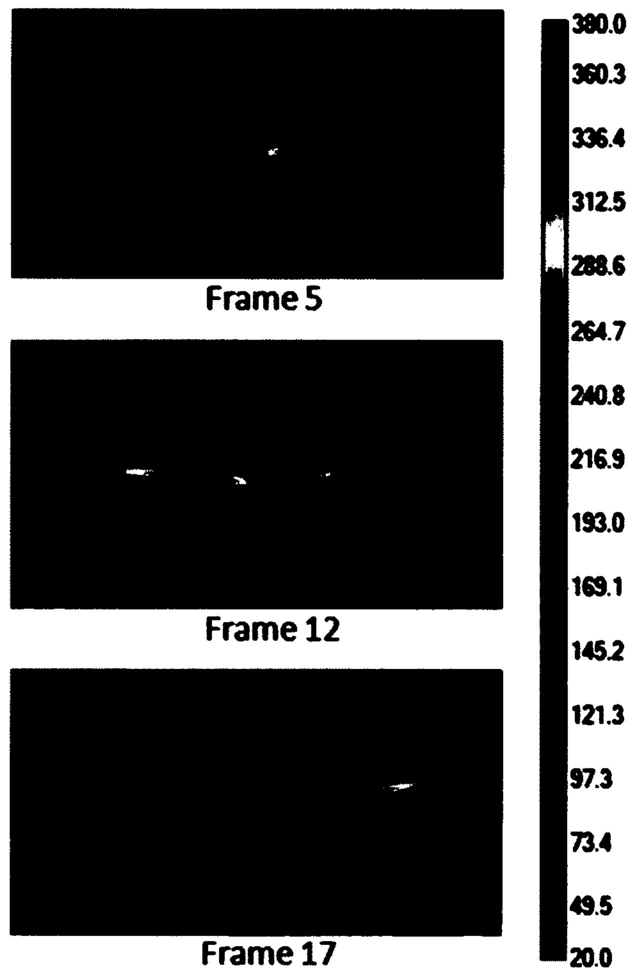

Figure 28: Maximum temperature location shifting from positive voltage die to the negative voltage die (Fine grain structure specimen test1).

Note that this trend was observed for the other grain structures as well. This shifting in temperature may be caused by the changing load as the specimen is deformed as the amount of force compressing the specimen onto the die would affect the electrical contact at the die/specimen interface. The 20[N] preload was applied for this reason to provide enough force to make sufficient contact between the specimen and the die. Higher preloads would have produced a better contact but any load higher than 20[N] could plastically deform the specimens.

A similar trend was observed in the copper wire compression tests. An example of one test is shown in Figure 29. Note that the temperature at the upper platen/specimen interface is higher than anywhere else within the specimen.

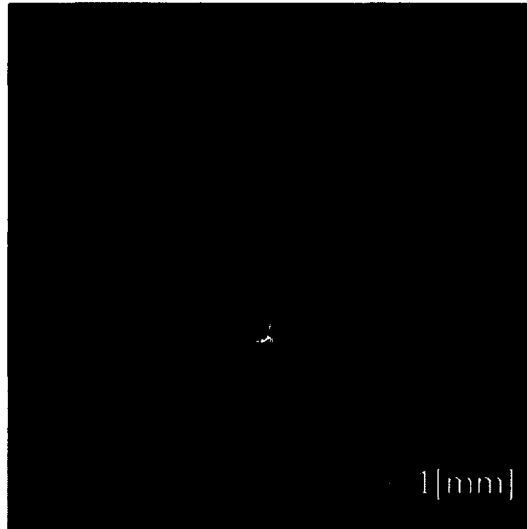

Figure 29: Higher temperature at the positive voltage platen.

For both forming processes, the trend of higher temperature at the positively charged interface was observed at least initially. Although the convention for electrical current flow is from positive to negative, the electrons physically move from negative to positive. However, when the leads were switched, the higher temperature did not switch to the positive side and the thermal profiles were very similar.

4.1.4 Problems with Measuring Springback For the Microbending Tests

An attempt was made to collect DIC images at the end of the microbending tests and after the specimen was unloaded to obtain springback data. However, several complications arose. After microbending was complete and the specimen was unloaded, many of the specimens would remain wedged between the dies. Therefore the springback of the specimen could not be measured accurately as the specimen couldn't elastically recover. When the specimen was removed from the die, the planar orientations as well as location

of the specimen were shifted so the DIC system could not track the deformation. Some specimens (in particular the fine grain samples) did stick to the end of the punch as they were unloaded. But this effect was too inconsistent to provide a sufficient amount of springback data.

4.1.5 Force Peaking in Three Point Bending

For both the EA and non-EA processes, the trend of the force peaking at a consistent displacement for each grain structure was observed. In past research, Wang et al. (1992) created an analytical model to predict the force displacement profile for three point bending. The model proposes that the bending force (i.e., punch load P) is related to three main factors. First, material properties of the specimen represented by the thickness t, strain hardening exponent n-value, strength coefficient K-value, and the plastic anisotropy index F-value. Second, specimen and tooling parameters denoted by the radii of the punch R_p and die R_d as well as the die opening L_d. Finally, the process parameters, represented by the bending angle θ, punch displacement d, and the friction coefficient μ. Their final equation was

$$P = \frac{\frac{KF^{n+1}}{2+n} wt^2 \left(\frac{t}{2R_p}\right)^n \left(1 + \frac{3n+2}{2n+3} \frac{t}{2R_p}\right)}{L_d\left[\left(1 - \frac{R_d}{L_d}\sin\theta\right) + \frac{\tan\theta - \mu}{1 + \mu\tan\theta}\left(\frac{d}{L_d} - \frac{R_d}{L_d}(1-\cos\theta)\right)\right]}. \quad (3)$$

For the peak to occur at a different displacement and value, at least one of these three factors would have to be changed. Upon close inspection of the FLIR data which shows the bending process, there were no changes in the tool parameters during deformation and the only process parameter that would change would be the friction coefficient. Therefore the major change can be assumed to be within the material

properties. With increases in temperature, K, n, and $\underline{F}$ would decrease. While these parameters appear in the numerator of this equation, n also appears in some denominators. Therefore, the exact effect on the punch force was not able to be determined without specific values.

4.1.6 Thermal Elongation

One of the purposed causes of the initial force plateau observed in the EA process was thermal elongation of the specimen. To investigate this, the thermal elongation was calculated using

$$\frac{\Delta L}{L} = \alpha_L \Delta T \tag{4}$$

where the elongation ΔL is related to the change in temperature ΔT by α_L (19[$\frac{10^{-6}}{C^o}$] for brass at 20[°C]). At a temperature of 400[°C] the elongation would only be 7.2[μm] and therefore would not be sufficient to describe the force plateau observed across the 40[μm] of displacement (shown in Figure 16).

CHAPTER 5

CONCLUSIONS

5.1 Three Point Microbending

The Electrical-Assisted (EA) process caused the strain gradients through the thickness of the specimens to be consistent for the coarse grain structure tests and lowered the deviation for all grain structures. The application of current had the largest effect on the force data for specimens with finer grain structures, especially within the first 0.5[mm] of displacement. This could possibly agree with the theory that the current aids dislocations motion past obstacles such as dislocations, grain boundaries, etc. If there are more grain boundaries and dislocations piled up in the finer grained microstructure, then the application of current would affect the forces more compared to the coarser grained structures as observed in the data. However, the typical effect of EAF is a reduction in the forming forces. For this data set, a reduction in force was only observed for approximately the first half of the tests. This was caused by a shifting of the force-displacement curve during the high temperature spike at the beginning of the tests. The maximum force values actually exceeded the non-EAF force for the fine and medium grain structures.

Results show that the strain on the tension side of the specimen was higher than the strain on the compressive side. Thus, the neutral axis shifted during this microbending process. The neutral axis location decreased more as the grain size increased for both the non-EA and EA processes. This is believed to be caused by the more limited deformation of the coarser grains which decreases the neutral axis shifting. However, there was a

much smaller difference in neutral axis shifting between grain structures for the EA case. For the EA process, the dislocation motion of the coarse grains was aided thus causing the neutral axis shifting to be more uniform.

5.2 Copper Wire Temperature Tests

For the copper wire temperature tests, the C101 specimens with the coarse grain structures produced the highest temperatures with the application of electrical current compared to the other grain structures. In past research (Siopis and Kinsey,2010), the lowest flow stress reductions were also observed with the C101 coarse grain structure specimens. Therefore, based on the results from these static tests, the flow stress reduction cannot be explained by the increased temperature alone. While the copper wire tests did not include continuous deformation, the coarse specimens still had the highest temperature initially and throughout with the three point bending tests. It is believed although unsubstantiated that the inconsistent trend between temperature and grain structure for the copper wire tests was observed due to errors in the heat treatment of the fine and medium specimens. A trend between higher temperature and increased Zn content was observed with the brass alloys; however, the difference between alloys was only about 30[°C]

CHAPTER 6

FUTURE WORK

Overall, the electrical contact had a major effect on the temperature and repeatability of the electrically-assisted microbending tests. If these tests are to be performed again, a way to maintain constant electrical contact throughout the tests must be found. One possible way would be to change the forming process to uni-axial tension. The specimen would not move or slide with respect to the grip supplying the current and therefore the electrical contact would remain constant.

Higher temperatures were observed where the positively charged dies contacted the specimens. To see if this effect was caused by the charge of the die and not the specimen, tests similar to those that were run in CHAPTER 2 could be done. Only after the test the specimen would be flipped and the electrical current reapplied to see if there are still higher temperatures at the positively charged die. Alternatively, the cables supplying the charge could be switched while the specimen remains stationary.

REFERENCES

Solid State Technology, 2012, http://www.electroiq.com/articles/stm/2012/03/top-mems-suppliers-near-1-billion-in-annual-sales.html, Accessed December 2012

Semi, 2012, http://www.semi.org/en/p044528, Accessed December 2012

Geiger, M., Kleiner, M., Eckstein, R., Tiesler, N., and Engel, U.,"Microforming", CIRP Ann., 50(2), 2001, pp. 445-462.

Hansen, N., 1977. "The effect of grain size and strain on the tensile flow stress of Aluminum at room temperature", Acta Metallurgica, Vol. 25, pp. 863-869.

Asad, A.B.M.A., Masaki, T. Rahman, M., Lim, H.S., Wong, Y.S., "Tool-based micro-machining", J. of Mater. Process. Technol., 192-193, 2007, pp. 204-211.

Raulea, L.V., Goijaerts, A.M., Govaert, L.E., and Baaijens, F.P.T., "Size effects in the processing of thin metal sheets," J. Mater. Process. Technol., 115, 2001, pp. 44-48.

Korkolis Y. Wang, L. and B.L. Kinsey, "Investigation of strain gradients and magnitudes during microbending". submitted to the Journal of Manufacturing Science and Engineering., 2011.

McNeal-T. A. Roth-J.T. Green, C. R. "Springback elimination for al-6111 alloys using electrically assisted manufacturing (eam)". North American Manufacturing Research Conference Proceedings (NAMRC), pages 1-8.

Jeen-Terng Gau, Chris Principe, Miao Yu, "Springback behavior of brass in micro sheet forming". Journal of materials processing technology(ELSEVIER), 191 (2007) 7-10.

Diehl, A., Engel, U., Geiger, M., "Investigation of the spring-back behavior in metal foil forming" Proceedings of the 24th IDDRG-conference, Besancon, Frankreich(2005)

Bungent, C., Mears, L., Salandro, W.A., "Modeling and quantification of the elctroplastic effect when bending stainless steel sheet metal" International Manufacturing Science and Engineering Conference (MSEC), 2010

Kronenberger-T. J. Perkins, T. A. and J. T. Roth, "Metallic forging using electrical ow as an alternative to warm/hot working". Journal of Maufacturing Science and Engineering, 129(1),:84-94, 2007.

Bunget, C., Salandro, W., Mears, L. (2011), "Several Factors Affecting the Electroplastic Effect During an Electrically-Assisted Forming Process," ASME Journal of Manufacturing Science and Engineering Special Issue on Forming Technologies

Jones, J.J., Mears, L., and Roth, J.T. (2012) "Electrically-Assisted Forming of Magnesium AZ31: Effect of Current Magnitude and Deformation Rate on Forgeability," ASME J. of Manuf. Sci. and Eng. 134: 034504-1 - 034504-7."

Jones, J.J., Mears, "A process comparison of simple stretch forming using both conventional and electrically-assisted forming techniques" International Manufacturing Science and Engineering Conference (MSEC), 2010

Bottomley, J.T., "Expansion with rise of temperature of wires under pulling stress" The Electrical Engineer, pp 19, 1889

Conrad, H., 2000, "Effects of Electric Current on Solid State Phase Transformations in Metals," *Mater. Sci. Eng., A*, 287, pp. 227-237.

Roylance, D., 2001, "The Dislocation Basis of Yield and Creep," *Modules in Mechanics of Materials*, available at http://web.mit.edu/course/3/3.11/www/modules.html.

Yao, L. Hong, C., Yunqou, G., and Xinbin, H., 1996, "Effect of Electric Current Pulse on Superplasticity of Aluminum Alloy 7475", *Transactions of NFsoc*, 6(1), pp. 77-80.

M. Siopis and B.L. Kinsey, "Experimental investigation of grain and specimen size effects during electrical-assisted forming" Journal of Manufacturing Science and Engineering, 132(2), 1004:1-7, 2010.

Dzialo, C.M., Kinsey, B.L., Siopis, Weinmann, K.J., "Effect of current density and zinc content during electrical-assisted forming of copper alloys" Journal of materials processing technology(ELSEVIER)

Wang C., Kinzel G.L. and Altan T.,"Plane Strain Sheet Bending – Fundamentals and Applications: Part I" Report No. ERC/NSM-S-92-15, The Ohio State University, Columbus, Ohio, 1992.

Cubberly, W.H., "Metals Handbook Ninth Edition Volume 2 Properties and Selection: Nonferrous Alloys and Pure Metals" Page 325, American Society for Metals Columbus, Ohio, 1978.